Rydberg states of rubidium in crossed electric and magnetic fields

F. Penent,* D. Delande, and J. C. Gay
Laboratoire de Spectroscopie Hertzienne de l'Ecole Normale Supérieure,
Université Pierre-et-Marie-Curie, Tour 12, E01, 4 place Jussieu, 75252 Paris Cedex 05, France
(Received 13 April 1987; revised manuscript received 30 December 1987)

The results of an experimental study of the Rydberg spectrum of rubidium in crossed electric and magnetic fields are reported and compared with theoretical predictions. The present investigations have been conducted in the low-field regime in which the paramagnetic and linear Stark interactions are perturbations to the Coulomb energy. When quantum-defect corrections are negligible, the SO(4) symmetry of the Coulomb interaction organizes the hydrogenic energy spectrum according to the law $E_{n,k}=-R/n^2+\hbar k(\omega_L^2+\omega_S^2)^{1/2}$, where k is an integer such that $-(n-1)\leq k\leq(n-1)$, and ω_L,ω_S are, respectively, the Larmor and linear Stark frequencies. The experimental evidence for such a quantization is presented in rubidium Rydberg series using Doppler-free two-photon spectroscopy. The role of quantum defects is incorporated into the theory and experimentally demonstrated.

INTRODUCTION

Advances in tunable laser sources have allowed for a few years the controlled and highly efficient production of atoms in high Rydberg states. These Rydberg systems are a nearly perfect realization of Coulombic systems in three dimensions. Studies of their properties under static electric and/or magnetic external fields proved fruitful. Especially, the combined experimental-theoretical efforts in the area led to considerable progress in the understanding of basic problems such as the Stark effect and diamagnetism.[1]

Understanding the physics of atoms in combined electric and magnetic fields is still a challenge, due to the lack of any constant of motion. Physical implications are important; for example, in vapor-phase conditions, applying a **B** field to atoms results in the appearance of the so-called motional electric field in the atom rest frame. Good knowledge of the crossed-fields situation is thus needed, even for dealing with atomic diamagnetism.[2] Several phenomenological models have also pointed out the existence of a double-well behavior,[3–5] modeling an atomic Penning trap, which suggests the possible existence of new classes of atomic states or resonances.[6]

The experimental and theoretical results which are reported in this paper can be considered as the first step towards the solution of the crossed-fields problem. We consider a situation in which the electric and magnetic perturbations are small corrections to the Coulomb energy.

The quantum theory of this low-field regime was established by Pauli in 1926.[7–11] In this regime, the SO(4) symmetry of the Coulomb problem is broken by the external field perturbation. The analysis of our experimental results makes use of these concepts on Coulomb symmetry which are recalled in Sec. I. In Sec. II, the role of non-Coulombic corrections to the potential is considered. The experimental setup is described in Sec. III and the experimental technique in Sec. IV. In Sec. V, experimental results are discussed and interpreted.

Atomic units are used throughout the text. Writing $e^2=q^2/4\pi\varepsilon_0$ (q the electron's charge) and with R the Rydberg constant, the unit of energy is $2R=me^4/\hbar^2$. The atomic unit of electric field is thus $E_c=m^2e^6/|q|\hbar^4=5.14\times10^9$ V/cm. The atomic unit of magnetic field is $B_c=m^2e^4/|q|\hbar^3=2.35\times10^9$ G. In the following, the fields are assumed to be parallel to the z axis (**B** field) and parallel to the x axis (**E** field).

I. HYDROGEN ATOM IN WEAK CROSSED FIELDS

Assuming the proton infinitely massive, the nonrelativistic Hamiltonian to first order in (**E**, **B**) fields is

$$H=H_0+W\ ,$$
$$H_0=p^2/2m-e^2/r\ , \tag{1}$$
$$W=-(q/2m)\mathbf{B}\cdot\mathbf{l}-q\mathbf{E}\cdot\mathbf{r}$$

in the cylindrical gauge. $\mathbf{l}$ is the angular momentum ($\mathbf{l}=\mathbf{r}\times\mathbf{p}$). The paramagnetic and dipolar electric terms are perturbations to the Coulomb Hamiltonian H_0. The diamagnetic interaction is neglected.

A. SO(4) treatment of the low-field regime

The solution of (1) requires us to apply perturbation theory to the n^2 degenerated n Coulomb shell. The solution is readily deduced *in closed form*, introducing the generators of the SO(4) symmetry group of the nonrelativistic Coulomb interaction. Writing **a** the Runge-Lenz vector with

$$\mathbf{a}=(-2mH_0)^{-1/2}[(\mathbf{p}\times\mathbf{l}-\mathbf{l}\times\mathbf{p})/2-me^2\mathbf{r}/r]\ , \tag{2}$$

the set ($\mathbf{l}$, **a**) is well known to build the six components of an angular momentum $\mathcal{L}$ in a four-dimensional space.[8,9,12] The components of $\mathcal{L}$ commute with the Coulomb Hamiltonian H_0 which establishes the SO(4) invariance of the bound spectrum.

In a given n shell, $\mathbf{r}$ identifies with $-\frac{3}{2}n\mathbf{a}$ (the so-called "Pauli replacement"[7]) and the perturbation W is expressed as a linear function of the generators

$$W=\omega_L\cdot\mathbf{l}+\omega_s\cdot\mathbf{a}\ , \tag{3}$$

where $\omega_L=-q\mathbf{B}/2m$ is the Larmor frequency and $\omega_S=\frac{3}{2}(4\pi\varepsilon_0\hbar/mq)n\mathbf{E}$ is the linear Stark one.

B. Crossed-fields spectrum in the low-field limit

The conventional way for dealing with Eq. (3) is to introduce the two operators

$$\mathbf{j}_{1/2}=\tfrac{1}{2}(\mathbf{l}\mp\mathbf{a})\ . \tag{4}$$

They fulfill the commutation relations $[j_{il},j_{jk}]=i\delta_{ij}\varepsilon_{lkm}j_{im}$ (with $i,j=1,2$) of two commuting angular momenta in three dimensions. Furthermore $j_1^2=j_2^2=j(j+1)$ and $j=(n-1)/2$ follow directly from $\mathbf{l}$. $\mathbf{a}=0$ and $l^2+a^2+1=-1/(2H_0)$. Hence, the perturbation W can be written down,

$$\begin{aligned}&W=\omega_1\cdot\mathbf{j}_1+\omega_2\cdot\mathbf{j}_2\ ,\\&\omega_{1/2}=\omega_L\mp\omega_S\ .\end{aligned} \tag{5}$$

The quantization scheme is $(j_1^2j_2^2\,j_{1\omega_1}j_{2\omega_2})$, leading to

$$\begin{aligned}&E_{nk}=-\frac{1}{2n^2}+k\omega\ ,\\&-j\le m_i\le j\ ,\\&-(n-1)\le k=m_1+m_2\le(n-1)\ ,\end{aligned} \tag{6}$$

where $\omega=(\omega_S^2+\omega_L^2)^{1/2}$ is the modulus of ω_1 and ω_2.

The n^2-degenerate manifold is thus split into $(2n-1)$ sublevels labeled with the integer k which measures the sum of the quantized projections of $\mathbf{j}_1$ and $\mathbf{j}_2$ onto, respectively, the ω_1 and ω_2 axes (cf. Figs. 1 and 2). The remaining degeneracy of the k sublevel is $n-|k|$.

In 1984 we first noticed[13] that another description is possible. The operator $\boldsymbol{\lambda}(a_x,a_y,l_z)$ (Refs. 13–16) is a three-dimensional angular momentum, the eigenvalues of which are $\lambda^2=\lambda(\lambda+1)$ with $0\le\lambda\le(n-1)$. The perturbation W is expressed as

$$W=(\omega_L+\omega_S)\cdot\boldsymbol{\lambda}=\omega_2\cdot\boldsymbol{\lambda}=k\omega \tag{7}$$

and is diagonal in the $(j_1^2j_2^2\lambda^2\lambda_{\omega_2})$ quantization scheme. Obviously, the degeneracy of the $\lambda_{\omega_2}=k$ sublevel on λ is $n-|k|$ according to $|k|\le\lambda\le(n-1)$.

C. Some characters of the eigenfunctions

The angle α between ω_2 and $\mathbf{B}$ field plays an important role. Its expression is:

$$\alpha=\tan^{-1}(\omega_S/\omega_L)\ . \tag{8}$$

The Zeeman ($\alpha=0$) and linear Stark regimes ($\alpha=\pi/2$) are limiting cases of the crossed-field quantization. But from (6) or (7), the energy diagram structure is the same whatever the α value.

The eigenfunctions at fixed (E,B) are deduced through a rotation with axis $\mathbf{n}$ along $\mathbf{B}\times\mathbf{E}$ from either limits. Their expressions from the Zeeman limit are (see Appendix A)

$$\begin{aligned}&|j_1^2j_2^2m_1m_2\rangle_{\omega_{12}}=e^{i\alpha\mathbf{j}_1\cdot\mathbf{n}}e^{-i\alpha\mathbf{j}_2\cdot\mathbf{n}}|j_1^2j_2^2m_1m_2\rangle_z\ ,\\&|j_1^2j_2^2\lambda k\rangle_{\omega_2}=e^{-i\alpha\boldsymbol{\lambda}\cdot\mathbf{n}}|j_1^2j_2^2\lambda k\rangle_z\ .\end{aligned} \tag{9}$$

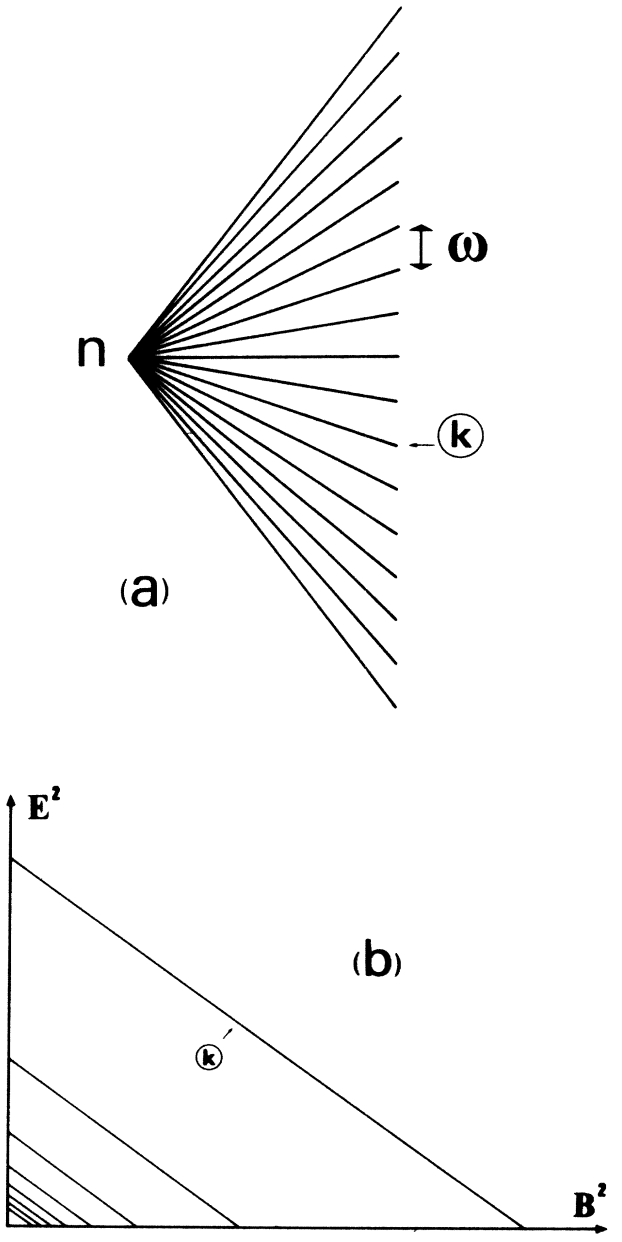

FIG. 1. Crossed-field quantization in the low-field regime for a pure Coulomb situation. The energy surface depends on the magnitude of the E and B fields. Sections at constant $\mathbf{E}/\mathbf{B}$ (or ω_S/ω_L) display the structure of the manifold in energy (a), viz., a set of $(2n-1)$ sublevels equally spaced with $\omega=(\omega_S^2+\omega_L^2)^{1/2}$, each k sublevel being $n-|k|$ times degenerate. Sections of the energy surface at constant energy (b) display the behavior of the energy levels as a function of E and B, which are straight lines in a (E^2,B^2) plot.

The generator being $\lambda_y = a_y$, such a rotation is *not* of the usual geometrical type (the generator of which is a component of $\mathbf{l}$).[13]

Finally, the parity Π_z along the **B** field is a symmetry operation. In the $(j_1^2 j_2^2 \lambda^2 \lambda_{\omega_2})$ scheme, the eigenstates have defined $\Pi_z = (-)^{n-\lambda-1}$. Conveniently symmetrized expressions in the $(j_1^2 j_2^2 j_{1_{\omega_1}} j_{2_{\omega_2}})$ scheme are odd or even under the exchange of $\mathbf{j}_1$ and $\mathbf{j}_2$.

II. ALKALI-METAL ATOMS IN CROSSED FIELDS: THE INCOMPLETE SO(4) MANIFOLD APPROACH

In alkali-metal Rydberg atoms, non-Coulombic corrections to the potential induce a breaking of the SO(4) symmetry. This leads to quantum defects of the zero-field energy levels which are usually important for $l \leq 2$ states [e.g., in Rb, $\delta(S)=3.13$, $\delta(P)=2.64$, $\delta(D)=1.35$, while $\delta(F)=0.017$].

As long as the external-field perturbation is small compared with quantum-defect corrections δ/n^3, the S, P, and D states present a nonhydrogenic behavior in the field, exhibiting the orbital Zeeman effect, diamagnetic and quadratic Stark shifts. But states with $l \geq 3$ with negligibly small quantum defects are *nearly degenerate.* They build an *incomplete*[17] hydrogenic manifold, with (n^2-9) degeneracy.

A. Quantization of the incomplete manifold in crossed fields

The use of the resolvent formalism[17–22] allows us to understand most of the structure of the energy diagram at low fields, while relying on symmetry considerations[18,20] (Appendix B). The energy levels in crossed fields are matched through the formula[18–20]

$$E_{nk^*} = -\frac{1}{2n^2} + W_{nk^*} , \tag{10}$$

with $W_{nk^*} = k^*(\omega_L^2 + \omega_S^2)^{1/2}$; k^* plays the role of an effective quantum number.

Most of the states of the incomplete manifold are still *exactly* quantized according to the hydrogenic law [Eq. (7)]. Hence, k^* in Eq. (10) is an integer and constant whatever the (**E**,**B**) fields. These states are not perturbed by the incomplete character of the manifold. Hence, they are not coupled through W to the (S,P,D) states.

The states coupled through W to the (S,P,D) states[18] contain a nonzero component on the $l=3$ wave functions. Their behavior slightly departs from the hydrogenic law: k^* in Eq. (10) is not an integer and depends on the (**E**,**B**) fields.

Coupling is through the *Stark interaction* to the *five* "D" channels. Hence, for each k value, there are only five states (three even Π_z and two odd Π_z states) which should depart from the hydrogenic law (k^* noninteger). The $(n-|k|-5)$ remaining ones are unperturbed. Furthermore, the Zeeman interaction leads to no coupling, which explains why the behavior in the Zeeman limit is hydrogenic (k^* integer, see Sec. II B).

B. Zeeman-Stark transition in the diagram

The plot in Fig. 3 represents the variations of k^* against $\alpha = \tan^{-1}(\omega_S/\omega_L)$ for the $n=34$, even Π_z, incomplete manifold. For the sake of clarity, the states exactly quantized according to the hydrogenic law are not represented (they would be represented with $(n-|k|-5)$ straight lines, $k = c^{\text{st}}$, for each integer k value).

The departure from the hydrogenic behavior ($k^* = k + \delta k$ noninteger) becomes noticeable when

$$\frac{k}{n} = \sin[\alpha + \sin^{-1}(l^*/n)] . \tag{11}$$

This is established semiclassically in Appendix C. l^* is the minimum value of l contained in the manifold (for $l^*=0$ the manifold is complete).

C. Interaction between nonhydrogenic states and the incomplete manifold

A key point in connection with experimental studies reported in Secs. III–V lies in the analysis of the interactions between the nonhydrogenic states (S, P, and D) and the incomplete manifold.[18,19]

Obviously, the states of the manifold which are *exactly* quantized according to the hydrogenic law [Eq. (7) or (10) with k^* integer] are not coupled to the nonhydrogenic (S,P,D) states. The two sets of energy curves cross each other in the low-field regime.

The states quantized according to Eq. (10) (k^* noninteger, cf. Fig. 3) are coupled to the nonhydrogenic (S,P,D) states and lead to anticrossings of the energy curves.

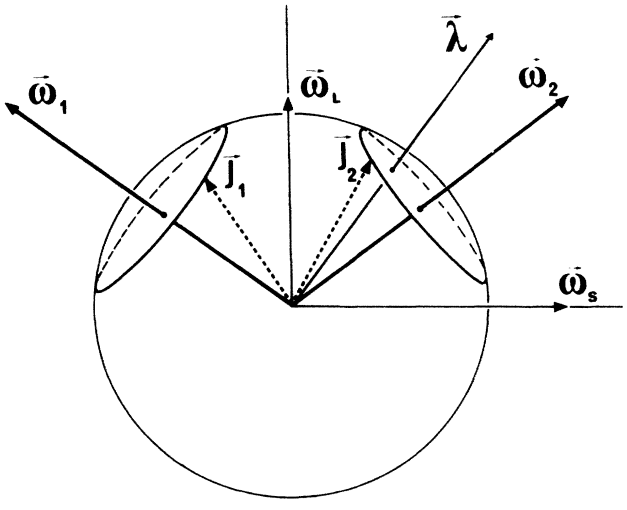

FIG. 2. Vectorial model of the Coulomb dynamics in a given n shell, based on the SO(4) symmetry. $\mathbf{j}_1, \mathbf{j}_2$ are the two commuting 3D angular momenta built from the Lenz vector **a** and the angular momentum. They are subjected to the constraints $j_1 = j_2 = (n-1)/2$, implying that their tips lie on a sphere. In crossed-field conditions, $\mathbf{j}_1$ and $\mathbf{j}_2$ precess around, respectively, ω_1 and ω_2, and $k = j_{1_{\omega_1}} + j_{2_{\omega_2}}$ is conserved. The angular momentum $\boldsymbol{\lambda}(a_x, a_y, l_z)$ also precesses around ω_2 (with $\lambda_{\omega_2} = k$). The angular velocity of precession is $\omega = (\omega_S^2 + \omega_L^2)^{1/2}$.

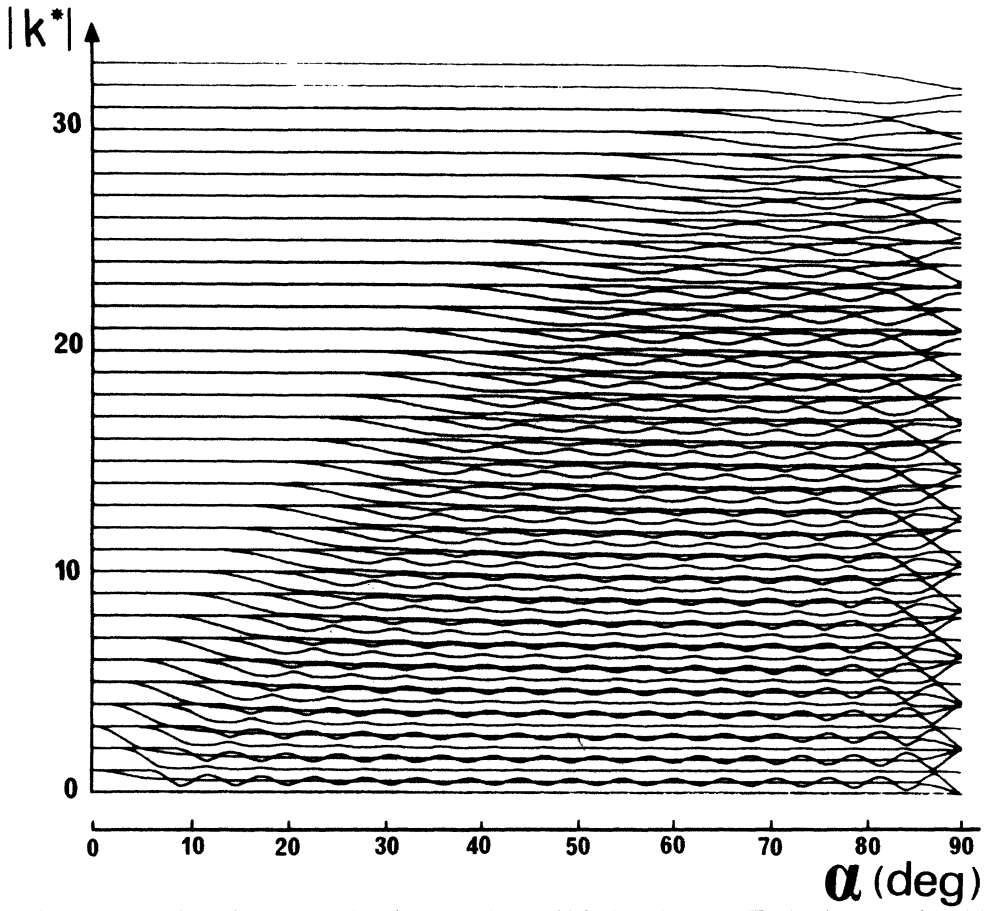

FIG. 3. Crossed-field quantization of an incomplete hydrogenic manifold ($n=34$, even Π_z) in the case of rubidium. The effective quantum number $k^*=W_{nk}*/(\omega_S^2+\omega_L^2)^{1/2}$ [Eq. (10)] is plotted against $\alpha=\tan^{-1}(\omega_S/\omega_L)$ (in degrees). States exactly quantized according to the hydrogenic law [Eq. (7)] would lead to $k^*=c^{ste}$ for each integer k value (not plotted). The plot thus characterizes the departures from the hydrogenic behavior for the states which are experimentally detected through anticrossings. The behavior is hydrogenic in the Zeeman limit ($\alpha=0$), then a transition region exists where usually three states leave the k submanifold. Variations of k^* are about (-1) up to the Stark limit ($\alpha=90°$).

The situation of the S series is of special experimental interest (cf. Fig. 4). The coupling through the Stark interaction is at third order in the **E** field and leads to sharp anticrossings. In the Zeeman limit, the anticrossings should disappear.[18]

III. EXPERIMENTAL SETUP

A schematic view of the experimental setup is shown in Fig. 5. cw dye-laser excitation of atomic rubidium using Doppler-free two-photon spectroscopy is performed under vapor-phase conditions. The Rb cell allows thermionic detection of the ions, produced from the Rydberg atoms.[18,19]

A. Tunable cw dye laser

This is an R6G, Ar^+-pumped ring dye laser[18,23] which delivers about 800 mW single-mode power at $\lambda\sim5900$ Å. The frequency is servo-controlled to within 1-MHz accuracy. Locking on an external Perot-Fabry cavity allows 140-GHz single-mode pressure scans of the frequency.

The frequency is measured to within 1-MHz relative accuracy by means of a 75-MHz free-spectral-range Perot-Fabry interferometer.

B. Rubidium cell and field arrangements

The cell with silica Brewster-angled windows contains the electrodes that allow the application of a small electric field (supplied with a battery) in the range 0–25 V/cm between a plate and a mesh spaced 4.2 mm apart (see inset of Fig. 5). Another closed compartment aside from the interaction region contains a 800-K heated tungsten wire, 0.15 mm in diameter, allowing this device to work as a thermoionic detector.[24,25]

The typical vapor pressure is about 10^{-2} Torr and kept low enough in order to limit chemical attack of the Brewster windows. The magnetic field is produced by means of air coils in Helmholtz positions giving up to 720 G. The earth field (about 0.2 G) is not compensated. The **E** and **B** fields are crossed to within 2°.

C. Doppler-free two-photon optical arrangement

The laser beam is focused into the interaction region by means of two lenses and retrofocused with a spherical mirror. A Faraday optical insulator avoids retrofocusing into the laser cavity. Experimental conditions for achieving efficient Doppler-free two-photon excitation have

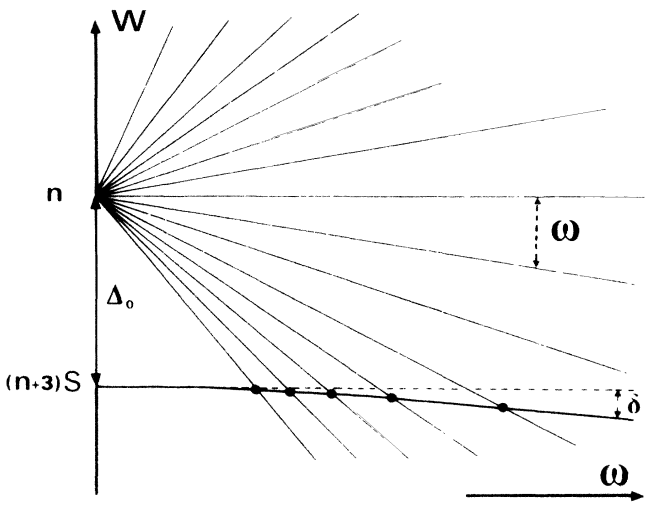

FIG. 4. Schematic representation of the crossed-field behavior for nonhydrogenic atoms. While the incomplete manifold is quantized according to the hydrogenic law [linear in $\omega=(\omega_L^2+\omega_S^2)^{1/2}$] the nonhydrogenic nS states have a smooth dependence of their energy curves, quadratic in E and B. From the anticrossings of the two systems of energy levels, it is possible to establish experimentally the quantization obeyed in the manifold at nearly constant energy (as $\delta \ll \Delta_0$) in conditions similar to those in Fig. (1b).

been extensively discussed.[26] It has been shown that most of the signal comes from atoms located in a volume defined by the waist of the laser beam and its Rayleigh length. In order to increase the electric field homogeneity to better than 1% we used a Rayleigh length of 2mm and a waist of 20 μm. Power shift and broadening are negligible.[18]

D. Two-photon line shapes and intensities in rubidium

Natural rubidium which is used in the experiments contains 72% ^{85}Rb (nuclear spin $I=\frac{5}{2}$) and 28% ^{87}Rb ($I=\frac{3}{2}$). The hyperfine structures of the ground state $5S_{1/2}$ are, respectively, 6.835 and 3.036 GHz, while completely negligible in high Rydberg states.

In contrast, the fine structure of the nP and nD levels is not negligible for $n \simeq 40$, while that of the $F,G,H,\ldots$ levels is smaller than 1 MHz.[19,27–30] Quantum defects are large for the nS, nP, and nD series. But they are negligible for the $nF,nG,nH,\ldots$ states with $l \geq 3$, which build an *incomplete manifold* (see Sec. II). So far as one considers only the nS and incomplete manifold states, both the fine and hyperfine structures are negligible. Thus one deals with a *purely orbital problem* in the excited states.

Doppler-free two photon transitions in zero field take place between the $5S$ and nD or nS states. Use of general formulas for the two-photon probability[26] leads to, for the ^{85}Rb $(5S_{1/2},F=3)\rightarrow nS_{1/2}$ transition,[28]

$$A=(1.2\times10^{-11})\left[\frac{\mathcal{P}}{S}\right]^2 n^{-3} \ (\text{sec}^{-1}) ,$$

where $(\mathcal{P}/S)$ is the power per unit surface (W/cm^2). The number of atoms excited per unit time is thus $N_{nS}\sim N_0(S/\mu)SA.$, where N_0 is the atomic density, S/μ the Rayleigh length, and S the surface of the laser beam at waist. One deduces $N_{37S}\simeq10^{10}$ atoms/sec, which assuming complete ionization and an amplification factor of 10^3 in the thermoionic detector leads to an electronic current of 10^{-6} A. This agrees with the experimental results.

E. Frequency modulated thermoionic detection

The Doppler-free two-photon absorption signal is Lorentzian-shaped (the Doppler-limited Gaussian part is unnoticeable). Using frequency modulation of the laser (around 230 Hz), the line shape is the derivative of the Lorentzian profile[19] as shown in Fig. 6. The depth of

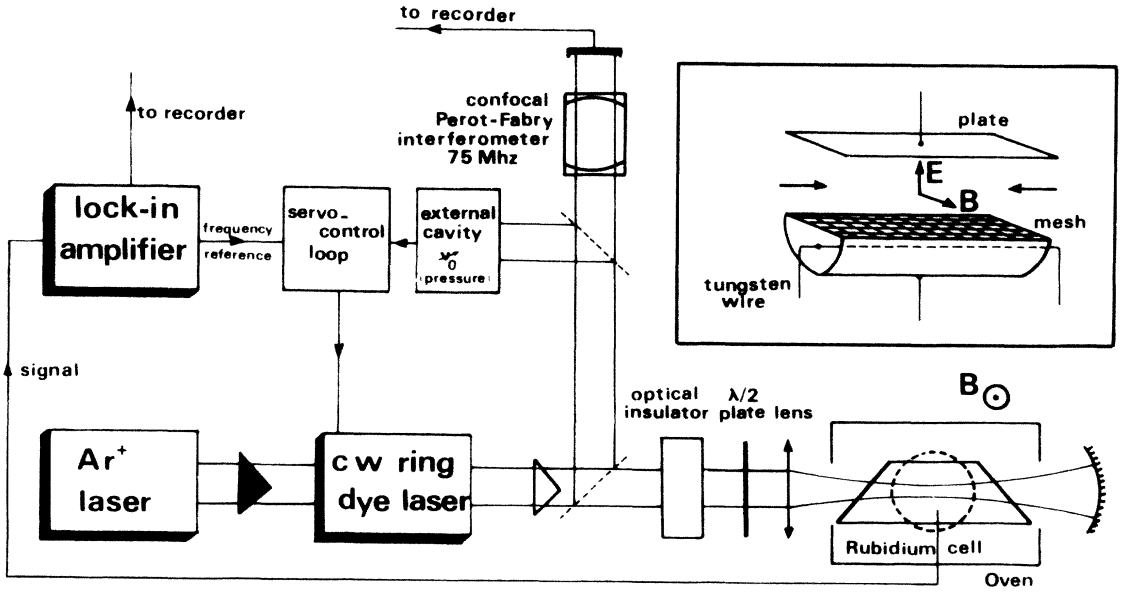

FIG. 5. Sketch of the experimental setup for Doppler-free two-photon excitation of rubidium Rydberg states in crossed fields. Details of the electrode arrangement in the Brewster-angled thermoionic detector are shown in the inset.

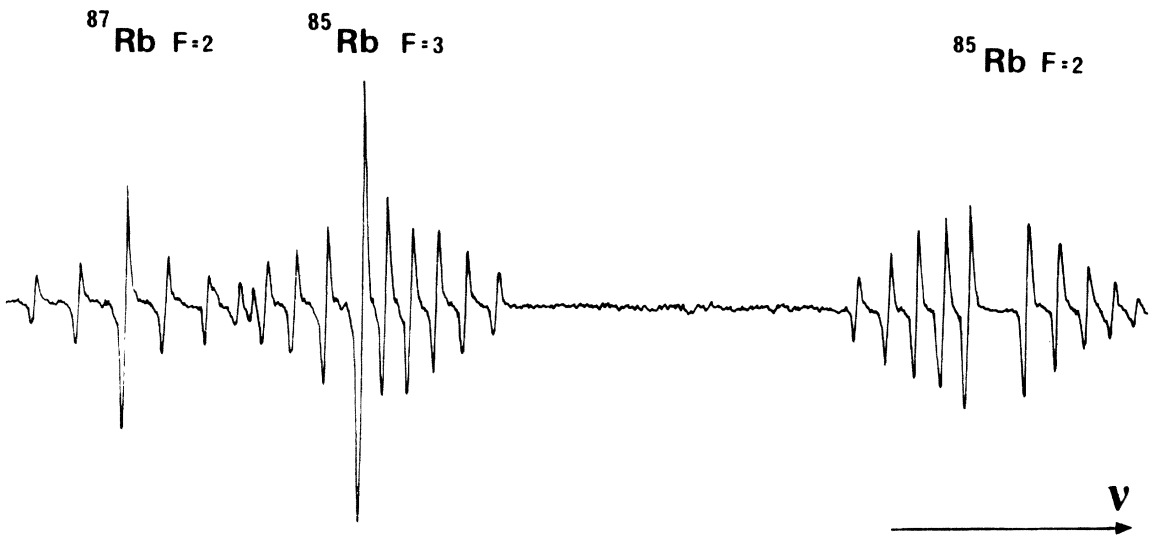

FIG. 6. Typical Doppler-free two-photon signal as obtained with frequency modulation of the laser. The signal is the derivative of the usual Lorentzian absorption signal. The plot has been taken with zero electric field and a magnetic field $B=294$ G on the $5S_{1/2}\rightarrow 37S$ two-photon transition. It exhibits the ground-state hyperfine Zeeman effect of rubidium and some of the isotopic hyperfine structure.

modulation (approximately equal to 5 MHz) is adapted to the (collisional) width of the curves which are red shifted by 5 MHz at maximum.[29] Stray electric field measured *in situ* are smaller than 20 mV/cm.

The use of frequency modulation of the laser combined with thermoionic detection leads to considerable enhancement of the signal-to-noise ratio. Using amplitude modulation, the time response of the detector is rather slow[25] (approximately equal to 50 msec) due to strong perturbations of the space charge by the laser. On the contrary, with FM techniques, the diode keeps the same permanent working point and the response extends to higher frequencies (up to 1 kHz). This also applies successfully to the detection of Doppler-limited profiles.[31]

F. Fields' calibration in the interaction region

Direct calibration of the fields in the interaction region has been deduced from measurements of the field dependence of the *nS*, *nP*, and *nD* "nonhydrogenic" series.

The magnetic field is measured to within 1 G accuracy in the interaction region, using hyperfine structure of the ground state and Zeeman splitting of the lines (see Fig. 6). Measurements of the diamagnetic blue shift of the *nS* state have been done on the $|F=3, m_F=\pm 3\rangle \rightarrow |nS, m_S=\pm\frac{1}{2}\rangle$ two-photon transition, which is free from paramagnetic shifts and decoupling effects. For the $37S$ state, the experimentally measured diamagnetic shift is $(3.27\pm0.02)\times10^{-4}$ MHz/G^2, in excellent agreement with nonhydrogenic perturbation theory[2] (3.28×10^{-4} MHz/G^2).

The electric field calibration to within 0.5% is deduced from the study of the Stark effect on the *nS*, *nP*, and *nD* series for n ranging from 30 to 47 and several M values. Theoretical reproductions of the Stark maps (through diagonalization on seven adjacent manifolds) to 5 MHz accuracy corresponds to input quantum defects with about four significant digits (values are extrapolated from previous measurements[18,28]). Such a sensitivity arises from a partial compensation in the quadratic Stark shifts. For example, the *nS* Stark shifts come from the interaction with the $(n+2)P$ and $(n+1)P$ levels, which are nearly symmetrically located on either side of the *nS*.

Determination of structural parameters of rubidium (fine-structure and static polarizabilities, see Table I) are in good agreement with previous measurements.[29] Static polarizabilities scale approximately as n^7E^2 to within 2%. Independent confirmation of the electric field calibration has been drawn from studies of the linear Stark behavior (see Sec. V A).

IV. EXPERIMENTAL TECHNIQUES: FM ANTICROSSING SPECTROSCOPY

Direct optical excitation of the states of the incomplete manifolds, being hardly possible at low fields, the key idea in the present experimental investigations on rubidium, is the one displayed in Fig. 4. The nonhydrogenic *nS* series present a weak-field dependence and are efficiently excited with two photons. Tracking of their anticrossings with the energy levels of the incomplete $(n-3)$ manifold, as a function of **E** and **B** fields, allows us to test the

TABLE I. Measured quadratic Stark shifts [MHz/(V/cm)^2].

$35D_{5/2}$	$M_j=\frac{5}{2}$	8.5±0.1
$40D_{5/2}$	$M_j=\frac{5}{2}$	22.3±0.2
$36P_{3/2}$	$M_j=\frac{3}{2}$	12.2±0.2
$41P_{3/2}$	$M_j=\frac{3}{2}$	33.6±0.3
$37S_{1/2}$	$M_j=\frac{1}{2}$	3.1±0.1
$42S_{1/2}$	$M_j=\frac{1}{2}$	7.5±0.2

Fine Structure

$35D$ $\Delta_{FS}=279\pm5$ MHz	$36P$ $\Delta_{FS}=2348\pm10$ MHz
$40D$ $\Delta_{FS}=184\pm5$ MHz	$41P$ $\Delta_{FS}=1525\pm10$ MHz

crossed-field quantization at nearly constant energy [in conditions similar to those in Fig. 1(b)].

A. Anticrossings spectroscopy on the nS series

The field dependence of the nS energy curve (see Sec. III F) is small such that $\delta \ll \Delta_0$ (see Fig. 4). Coupling with the manifold establishes at third order in **E**. The F state is approximately redistributed with $n^{-1/2}$ weight onto the manifold states. Hence the anticrossing width scales as $(n^2E)^3(1/n^3)^{-2}n^{-1/2}$. This leads to the weak value $V=aE^3n^{23/2}$ [with $a=1.1\times10^{-19}$ MHz/(V/cm)^3, in good agreement with numerical calculations, Sec. V] such that $V \ll (\omega_S^2+\omega_L^2)^{1/2}$. The interaction takes place in the weak-coupling regime and leads to well-separated anticrossings. This is actually valid for n values between 30 and 45, with the present range of fields ($E \leq 20$ V/cm, $B \leq 700$ G).

FIG. 7. Tracking the anticrossing position between the $n=34$ incomplete manifold and $37S$ state in the electric field problem (**B**=**0**). The anticrossing with the ($n=34$, $k^*=-27.6$) linear Stark sublevel takes place for an electric field value $E=12.49$ V/cm. The widths of the anticrossings are of the order of 80 MHz. Due to the weakness of the coupling with the S state, the transfer of oscillator strengths takes place on a very small range of electric field. From top to bottom, electric field values (V/cm) are 12.87, 12.54, 12.52, 12.50, 12.47, 12.45, 12.40.

B. Experimental procedures and line shapes

The method was checked by testing the linear Stark behavior obeyed in the manifold. A typical signal corresponding to the $n=37S$ anticrossing with the $k^*=-27.6$ state of the $n=34$ incomplete manifold is shown in Fig. 7.

The method has been extended to the crossed-field situation. The only difference arises from the existence of several lines associated with the hyperfine Zeeman effect of the ground state. However, the *dominant* two-photon transition $|F=3, m_F=\pm3\rangle \rightarrow |nS, M_S=\pm\frac{1}{2}\rangle$ is not affected by the magnetic field. Especially, there is a cancellation of the electronic spin contribution.

This transition has been used for the measurements of the anticrossings positions. As shown in Fig. 3 of Ref. 19, it is hardly possible to resolve the two states under interaction. The passing through anticrossing is detected from the strong decrease of the signal.

C. Diabatic FM Doppler-free anticrossing spectroscopy

The previous method is well adapted to the detection of large anticrossings but becomes inefficient at vanishing widths. In this case we made use of another scheme allowing direct recording of the anticrossing positions at fixed electric field, on the (0–700 G) **B** field range. It takes advantage of the smooth variations of the nS diabatic energy curve with B. The laser frequency (which is modulated) is servo-locked on the $|F=3, m_F=+3\rangle \rightarrow |nS, m_S=+\frac{1}{2}\rangle$ atomic transition whatever the B field. This is conveniently achieved by adding a small (5 G) ac component (frequency 20 Hz) to the magnetic field. Further heterodyne analysis of the error signal allows (0–700 G) **B** field scans while the laser frequency is locked on the atomic transition.[18,19,31] The passing through anticrossings results in a perturbation of the energy curve of the nS state. This manifests as an error signal on the **B** field loop. The anticrossing signal is roughly the derivative of the FM Doppler-free one, or the second-order derivative of a Lorentzian curve, as shown in Fig. 8. Recording of the error signal directly gives the positions of the anticrossings as a function of the B field. Such a record for the $n=34$ manifold and the $37S$ state and $E=10.88$ V/cm is shown in Fig. 8.

V. CROSSED-FIELD QUANTIZATION OF THE INCOMPLETE MANIFOLD: EXPERIMENTAL RESULTS

The study has been based on the $37S$, $n=34$ and $42S$, $n=39$ anticrossings. From previous comments this supplies us with a picture of the crossed-field quantization on the orbital structure, at nearly constant electron energy.

A. Linear Stark behavior from anticrossing spectroscopy

The study of the linear Stark effect allows independent confirmation of the electric field calibration (Sec. III F)

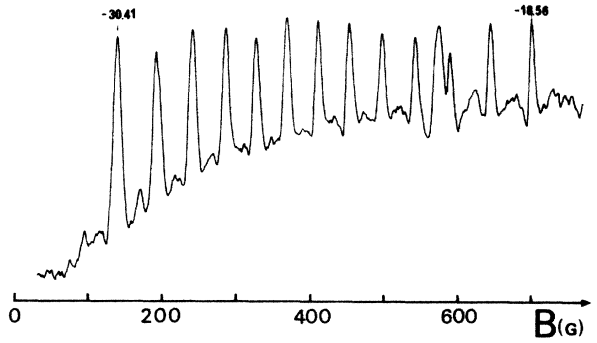

FIG. 8. Diabatic FM Doppler-free two photon signal from anticrossings between the $37S$ state and $n=34$ manifold, in crossed electric and magnetic fields. The two-photon laser line is locked on the $(5S_{1/2}, F=3, m_F=\pm 3) \rightarrow (37S, m_S=\pm\frac{1}{2})$ two-photon transition. The E field value is $E=10.88$ V/cm. The 0–700 G scan on the magnetic field allows direct recording of all the anticrossings with the $37S$ state. The signal (see text) is of absorption type and the assigned k^* values from left to right are $k^*=-30.41, -29.44, -28.47, -27.49, -26.52, -25.49, -24.48, -23.49, -22.51, -21.53, -20.49, -19.50, -18.56$. The parasitic signal seen around 575 G is due to accidental coincidence between two lines of ^{85}Rb and ^{87}Rb. The low-field variation of the background signal comes from the diamagnetic shift of the $37S$ state, the derivative of which scales as B.

TABLE II. Anticrossing positions and widths in the linear Stark regime and theoretical predictions (respective units are V/cm and MHz).

E_{expt}	E_{theor}	Width (Expt.)	Width (Theor.)
	$n=34$ manifold, $37S$ state		
10.67±0.05	10.67		50.7
11.51±0.05	11.53		66.7
12.49±0.05	12.51	80±10	86.1
13.66±0.05	13.64	110±10	114.3
15.02±0.05	15.00	140±20	154.2
16.70±0.05	16.66	210±20	212.4
	$n=39$ manifold, $42S$ state		
5.31±0.02	5.32		30.6
5.66±0.02	5.68		38.7
6.06±0.02	6.08		48
6.48±0.05	6.53		60.6
7.02±0.05	7.05		77.7
7.65±0.05	7.67	95±10	101.1
8.39±0.05	8.40	120±20	134
9.27±0.05	9.30	170±20	181
10.43±0.05	10.43	240±20	254
11.95±0.1	11.95	370±30	374
14.15±0.2	14.11	590±50	592

and experimental determination of the coupling V between the nS series and the states of the incomplete manifold through the widths of anticrossings. The anticrossings are detected in the vicinity (±100 MHz) of the nS energy curve (cf. Fig. 7). The positions and widths of the anticrossings are given in Table II. They agree to within 2% with the theoretical values.

B. Crossed-field quantization of the incomplete manifold: gross features

Compared to Ref. 19, results have been extended in a significant way through the use of the scheme described in Sec. IV C. Typical accuracies in the determination of the positions of anticrossings are 0.05 V/cm and 1 G.

Plotting in coordinates (E^2, B^2), the positions of the anticrossings with the nS diabatic energy curve result in a picture of the quantization obeyed in the incomplete manifold, at nearly constant energy. This is done in Figs. 9 and 10 where the points are the crude experimental results without any corrections.[18,19] This affords striking experimental evidence that the manifold states are approximately quantized according to Eq. (7), viz., $\Delta_0^2/k^2=(\omega_S^2+\omega_L^2)$, thus establishing the reality of the crossed field "Pauli" quantization (Δ_0 is the zero-field energy spacing, cf. Fig. 4). Furthermore, by comparing the slopes of the lines on the plots in Figs. 9 and 10, the n dependence of the linear Stark frequency ω_S is quite clearly exhibited.[19]

Each straight line on the plots is associated a given k sublevel, where k measures approximately the quantized value of the projection of the angular momentum λ [Eq. (7)] onto the $\omega_2=\omega_L+\omega_S$ axis (cf. Fig. 2). The eigenfunctions associated with the data in Figs. 9 and 10 do not share any common geometrical character. Nevertheless, the (E^2, B^2) organization nearly perfectly expresses the SO(4) symmetry of the Coulomb interaction.[13]

C. Detailed analysis of the crossed-field results

In Ref. 19, the data were dealt with according to the formula $\Delta^2=k_0^2(\omega_L^2+\omega_S^{*2})$, where k_0 was assumed to be constant whatever E and B, and measured at the disappearance of the anticrossings, close to the critical electric field value. ω_S^* was considered as a parameter giving the slopes in the (E^2, B^2) plot but actually was very close to the linear Stark frequency ω_S. However, ω_S^*/ω_S was slightly dependent on k_0. Although the determination of k_0 has been done in a region where the quantization is tending to the hydrogenic one, the method is not completely consistent, as the theoretical behavior of the energy levels (cf. Fig. 3) is not described with straight lines. This, in particular, becomes obvious with the extended set of experimental data we deal with here, where small nonlinearities in the (E^2, B^2) plots are clues that more detailed analysis is required, incorporating the role of quantum defects. Actually, in Sec. II D, we have shown that the states leading to anticrossings with the nS states should slightly depart from the hydrogenic crossed-field behavior. Their spectra obey Eq. (10) with $k^*=k+\delta k$. δk depends on the field strengths or on $\alpha=\tan^{-1}(\omega_S/\omega_L)$ [Eq. (8)] and measures the deviations from the hydrogenic law. k is the integer value of k^* at vanishing E field (hence, in the hydrogenic limit, see Secs. II C and II D).

Before extracting from the experimental data the value of k^* as a function of ω_S/ω_L one should correct it for the small variations of the energies of the nS state and for the second-order variations in E and B of the energies of

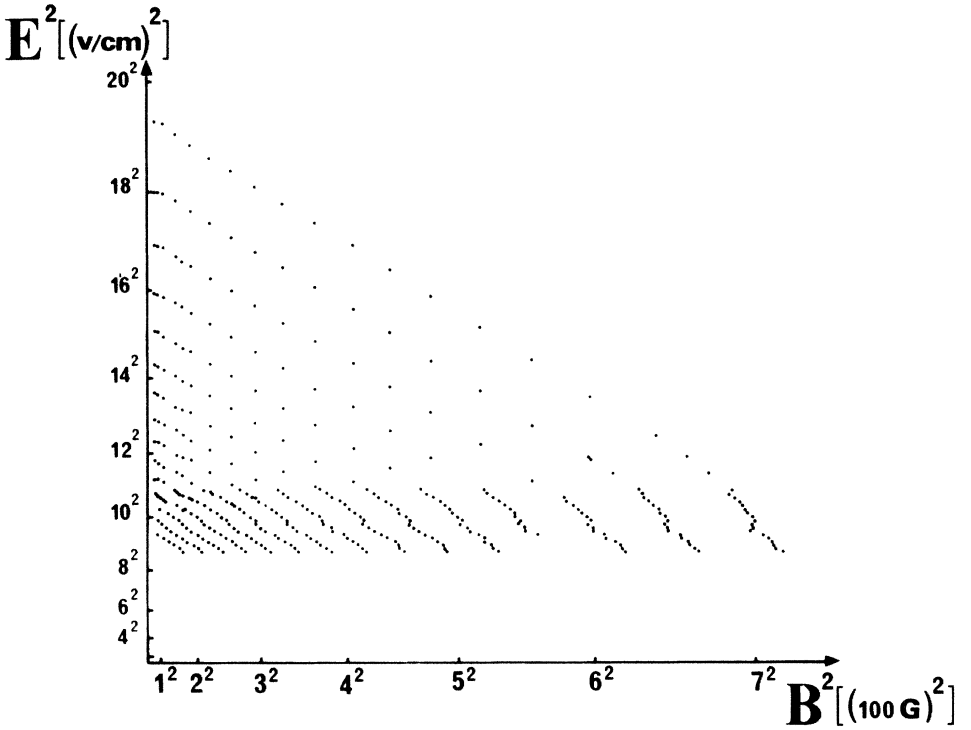

FIG. 9. (E^2,B^2) plot of the anticrossings between the $37S$ state and the $n=34$ incomplete manifold. This displays the crossed-field quantization at nearly constant energy [compare with Fig. 1(b)]. Each line is associated with a given k^* value which approximately measures the quantized projection of the SO(4) generator λ onto the ω_2 axis.

the incomplete manifold. The most important correction arises from the quadratic shifts of the nS diabatic energy curves experimentally determined in Secs. III F and V A. General arguments[18,20,31–34] applied to second-order corrections to the manifold energies for $n=34$ lead to a Stark red shift of -0.38 MHz/(V/cm)^2 and a diamagnetic blue shift of 3×10^{-4} MHz/G^2 (comparable to the one of the S state). These corrections here are about ±100 MHz at maximum.

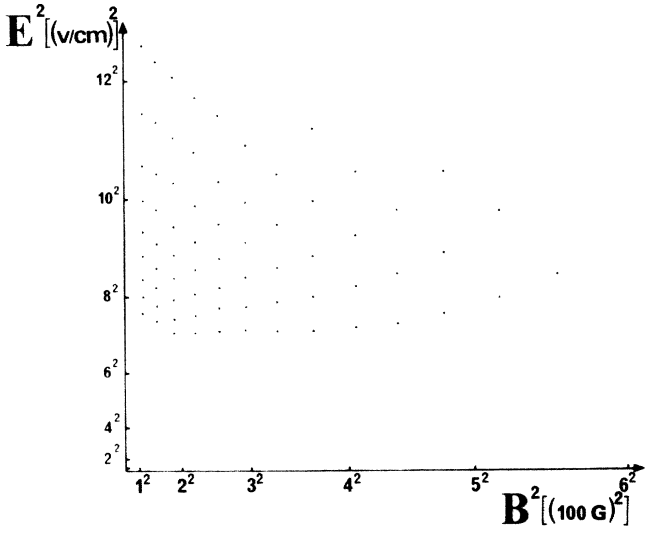

FIG. 10. (E^2,B^2) plot of the anticrossings of the $42S$ state and the manifold $n=39$. Comparison with Fig. 9 gives evidence of the Stark frequency scaling as nE (Ref. 19).

Finally, for the anticrossing data for the $37S$ state and the $n=34$ manifold, formula (10) should be amended as

$$|k^*|(\omega_S^2+\omega_L^2)^{1/2}=\Delta_0+\Delta_s+\Delta_B\ , \tag{12}$$

with $\Delta_0=22\,100$ $\Delta_s=2.76E^2$, $\Delta_B\simeq0$, $\omega_S=65.26E$, $\omega_L=1.3996B$, where the units are megahertz, Gauss, and V/cm. This allows us to deduce k^* as a function of $\alpha=\tan^{-1}(\omega_S/\omega_L)$. The experimental values for $n=34$ are plotted in Fig. 11.

The uncertainty in the determination of k^* is of the order of $\Delta k^*=0.10$. Limitations come from the uncertainty in the electric field calibration (0.5%) and from deviations from the quadratic behavior of the Stark shift of the nS state at high fields. Although it is small $[\delta(F)=0.017]$, the quantum defect of the F state also contributes to this uncertainty.

D. Evolution of the crossed-field quantization from the Zeeman to the Stark limit

As seen in Fig. 11, the value of $|\delta k|$ are slowly evolving from 0 to about unity as a function of ω_S/ω_L. This confirms that the experimental data in Figs. 9 and 10 refer to the regimes described in Sec. II where the crossed-field quantization is not perfectly hydrogenic.

The crossed-field quantization tends to the exact hydrogenic quantization when $\delta k\simeq0$. This is associated with the transition region in Fig. (3) [Eqs. (11)]. Actually, this is the region where anticrossings disappear, which explains why experimental values of $|\delta k|$ smaller than 0.1 have not been measured (cf. Fig. 11). On the plot in

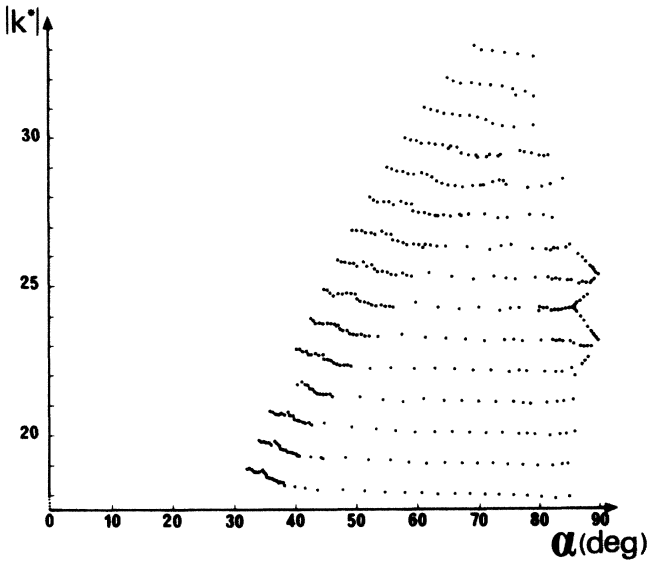

FIG. 11. Experimental plot of the effective quantum number k^* against $\alpha=\tan^{-1}(\omega_S/\omega_L)$ (scale in degrees; $37S$ state, $n=34$ manifold). The corrected experimental data can directly compare with theory in Fig. 3 (see Fig. 12 for a more detailed comparison). The agreement is excellent. As expected the anticrossings disappear when $\delta k^* \rightarrow 0$ (transition region where the quantization tends to the exact hydrogenic quantization).

Fig. 9 it is associated with a critical electric field value (cf. Appendix C) under which no measurements of this kind are possible.

As shown in Fig. 12 for $k=-19$ and $k=-20$, the experimental results are in excellent agreement with theoretical predictions. The maximum variations of δk are about -1 from the Zeeman to the Stark limit. They

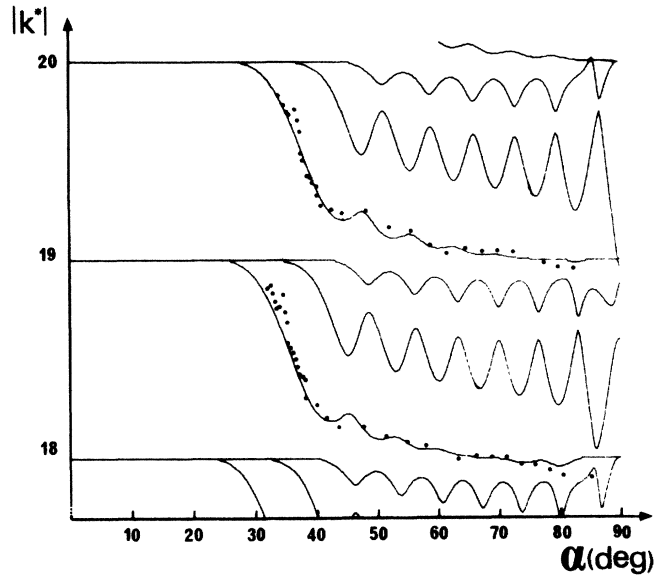

FIG. 12. Detailed comparison between theory and experiment for the $n=34$, $k=-20$, and $k=-19$ states of the incomplete manifold. Only one state among the three leaving the $(n-|k|)$-degenerated k submanifold is experimentally detected. It exhibits a departure from the hydrogenic crossed-field behavior with $|\delta k|=1$ at maximum.

mostly take place in the transition region in a small range of α values.

The plots of either Fig. 9 of Fig. 11 thus concern the most nonhydrogenic among the states of the incomplete manifold. Their behavior illustrate how the $n-|k|$ degeneracy of the k sublevel in crossed fields is partly removed due to non-Coulombic corrections to the potential. In comparison with Fig. 3, only one among the three sublevels leaving the k subshell is experimentally detected. This comes from the weakness of the coupling of the nS state with the others and can be accounted for using the resolvent formalism (Appendix B).

E. The Stark limit of the crossed-field spectrum

Figure 13 allows a comparison of theoretical and experimental results in this region where the data are far less regular and where the dominant physical effects come from non-Coulombic corrections to the potential and linear Stark effect (as $\omega_L \ll \omega_S$). This corresponds to B field values smaller than 50 G (α in the range $0.9\pi/2$ to $\pi/2$). In zero magnetic field only the states with $M=0$ are detected, through anticrossings with the nS ($M=0$) state (see Sec. V A). Applying a B field on the system allows to break the selection rule on the M value in this incomplete Stark manifold. Detection of states with k odd as well as even becomes possible. Hence, as shown in Fig. 13, the number of anticrossings experimentally detected *becomes twice the one* in the electric field alone.

There are strong interactions [cf. Fig. (13)] between sublevels when the magnetic interaction is branched, before the crossed-field quantization is established[17,19,22] for $\omega_L \simeq \omega_S$. This is consistent with previous measure-

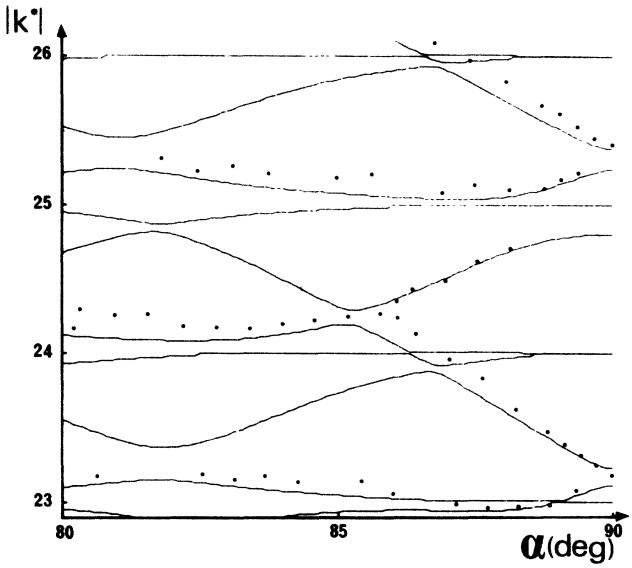

FIG. 13. Stark limit of the crossed-field spectrum of the $n=34$ incomplete manifold. The behavior of the energy levels is far less regular than in the intermediate range. Strong interactions in this regime manifest the passing from an incomplete manifold Stark quantization to the crossed-field quantization. The number of anticrossings with the $37S$ state, that is the number of experimental points on the plot, then becomes twice the number of anticrossings in the Stark limit ($\alpha=90°$).

ments[35] by Korevaar and Littman in conditions where $\omega_L/\omega_S < 0.1$. This also implies that linear extrapolation of the data in Fig. (9) at $B=0$ *cannot give the positions of the anticrossings in the Stark* (when dealing with nonhydrogenic atoms).

This agrees with our direct measurements in Table II and with those obtained on the first anticrossing by O'Sullivan and Stoïcheff.[29] But their further extrapolation at $B=0$ of our previous crossed-field results cannot be consistent.

VI. CONCLUSION ON THE CROSSED-FIELDS QUANTIZATION

We have thus experimentally established for the first time that the crossed-field spectrum of Rydberg atoms is organized according to the law $E_{n,k^*}=(-1/2n^2)+k^*(\omega_L^2+\omega_S^2)^{1/2}$ in the low-field limit. The value of k^* approximately measures the quantized projections of the angular momentum $\boldsymbol{\lambda}$ onto the $\boldsymbol{\omega}_2=\boldsymbol{\omega}_L+\boldsymbol{\omega}_S$ axis, making clear once more[13–16] its physical importance.

This is one of the most direct demonstrations of the SO(4) symmetry of the Coulomb interaction, although small effects of nonhydrogenic corrections to the potential lead to noninteger values of k^*.

ACKNOWLEDGMENTS

We would like to thank Dr. F. Biraben for invaluable help and advice during the early stage of the experimental work. Laboratoire de Spectroscopie Hertzienne de l'Ecole Normale Supérieure is associé au Centre National de la Recherche Scientifique, UA 18.

APPENDIX A: PROPERTIES OF THE CROSSED-FIELD EIGENFUNCTIONS

They belong to the two types of subgroup chains: type I,

$$\mathrm{SO}(4)=\mathrm{SO}(3)\otimes\mathrm{SO}(3)\supset\mathrm{SO}(2)\otimes\mathrm{SO}(2)\ ;$$

type II,

$$\mathrm{SO}(4)\supset\mathrm{SO}(3)\supset\mathrm{SO}(2)\ .$$

For the Coulomb problem, only self-conjugate representations[12] of SO(4) are realized [with $j_1=j_2=(n-1)/2$], which is associated with the second Casimir operator $\boldsymbol{l}\cdot\mathbf{a}$ being 0.

Type-I eigenfunctions are $(j_1^2 j_2^2 j_{1_{\omega_1}} j_{2_{\omega_2}})$ of a generalized parabolic type. If $\omega_1=\omega_2$ parallel to z axis, the $(j_1^2 j_2^2 j_{1_z} j_{2_z})$ coincide with the usual parabolic eigenfunctions to within a phase factor. l_z and a_z being defined from Eq. (4) one has

$$l_z=M=j_{1_z}+j_{2_z}\ ,$$

$$a_z=k=n_2-n_1=j_{2_z}-j_{1_z}\ ,$$

where (n_1,n_2) are the usual parabolic quantum numbers. Spatial representations in parabolic coordinates are known[13] and of a type separable in R^3. Use of Eq. (9) and conventional 3D angular momentum algebra allows us to deduce the expression of the generalized parabolic eigenfunctions.

The most-famous type-II eigenfunctions are $(j_1^2 j_2^2 l^2 l_z)$, which coincide to within a phase factor with the usual spherical basis. The parabolic and spherical types thus differ through a coupling of the angular momenta $\boldsymbol{l}=\mathbf{j}_1+\mathbf{j}_2$. This leads to (with $n=2j+1$)

$$|j_1^2 j_2^2 lM\rangle=\sum_{m_1 m_2}\left\langle\frac{n-1}{2}\,\frac{n-1}{2}\,m_1 m_2\,|\,1M\right\rangle \times|j_1^2 j_2^2 m_1 m_2\rangle\ ,$$

where the coefficients are the usual Clebsch-Gordan coefficients.

Another class of type-II eigenfunctions $(j_1^2 j_2^2 \lambda^2\lambda_z)$ is associated with the nonstandard coupling $\boldsymbol{\lambda}=(j_{2_x}-j_{1_x}, j_{2_y}-j_{1_y}, j_{2_z}+j_{1_z})$, where $\boldsymbol{\lambda}$ is a 3D angular momentum.[13–15] $\boldsymbol{l}$ and $\boldsymbol{\lambda}$ are interconnected through a SO(4) rotation[16] with generator $j_{1_z}=(l_z-a_z)/2$:

$$\boldsymbol{\lambda}=e^{i\pi j_{1_z}}\boldsymbol{l}e^{-i\pi j_{1_z}}\ .$$

Hence,

$$|j_1^2 j_2^2 \lambda\lambda_z\rangle=e^{i\pi j_{1_z}}|j_1^2 j_2^2 l l_z\rangle\ ,$$

which actually provides us with the expression (as well as spatial representation) in the parabolic or spherical basis. Consequently, the $(j_1^2, j_2^2, \lambda^2, \lambda_{\omega_2})$ eigenfunctions [see text and Eq. (9)] are expressed as

$$|j_1^2 j_2^2 \lambda M\rangle_{\omega_2}=e^{-ia a_y}e^{i\pi j_{1_z}}|j_1^2 j_2^2 l M\rangle$$

from the spherical basis with quantization along **B**.

In the Zeeman limit ($\omega_{1,2}=\omega_L$), the eigenfunctions are thus $(j_1^2 j_2^2 j_{1_z} j_{2_z})$ or $(j_1^2 j_2^2 \lambda^2\lambda_z)$. But $(j_1^2 j_2^2 L^2 L_z)$ is also a well-known solution. In the Stark limit, one finds with $\omega_{1,2}=\mp\omega_S$ either $(j_1^2 j_2^2 j_{1_x} j_{2_x})$ or $(j_1^2 j_2^2 \lambda^2\lambda_x)$. The latter provides us with a rotational-type description of the linear Stark effect.

B. APPENDIX B: QUANTIZATION OF AN INCOMPLETE MANIFOLD

The use of the resolvent formalism is an alternative to numerical calculations for dealing with the quantization of an incomplete manifold and more generally with symmetry-breaking perturbations.[17,19,20–22] At low fields, quantum-defect corrections make the n^2 states of the n manifold be split into two classes. Those with $l\geq 3$ are still energetically degenerated and build an incomplete ε_H manifold. It is incomplete in that the $l\leq 2$ states which build the $\varepsilon_{\mathrm{NH}}$ subspace are lacking compared to the hydrogenic situation.

Writing P (Q) the projector on the ε_H ($\varepsilon_{\mathrm{NH}}$) subspace with $P+Q=1$, the problem thus amounts to finding the eigenvalues $\{E=k^*\omega\}$ and eigenfunctions $\{|\psi\rangle\}$ of the restriction of the Hamiltonian PWP to the ε_H subspace. From (Ref. 21) one deduces

$$PWP\,|\,\psi\rangle = E\,|\,\psi\rangle\ , \tag{B1}$$

$$Q\,|\,\psi\rangle = 0\ . \tag{B2}$$

Elementary manipulations lead to the solution

$$Q(W-E)^{-1}QW\,|\,\psi\rangle = 0\ . \tag{B3}$$

Hence, $W\,|\,\psi\rangle$ is an eigenvector of $Q(W-E)^{-1}Q$ associated with a zero eigenvalue, which implies

$$\det[Q(W-E)^{-1}Q] = 0\ . \tag{B4}$$

As the dimension of $Q[W-E]^{-1}Q$ is $\dim\varepsilon_{NH}=9$ (rubidium case) and independent of n, computations have been reduced to a minimum. From Eq. (4) the perturbed spectrum is bounded with ($k^*>0$)

$$k-3\le k^*\le k\le(n-1)\ ,$$

while from Fig. 3 and numerical calculations the fluctuation δk^* is -1 at maximum.

Further reduction of Eq. (3) can be performed by exploiting the symmetries of W. Considering the product of time reversal and parity operations, the incomplete manifold is shown to be symmetrical around $k=0$.

The parity Π_z along the B field is a symmetry operation. Hence (3) and (4) should be considered in even $\varepsilon_{NH}(+)$ [$\dim\varepsilon_{NH}(+)=6$] or odd $\varepsilon_{NH}(-)$ [$\dim\varepsilon_{NH}(-)=3$] subspaces.

Finally, the ε_H and ε_{NH} subspaces are coupled through the electric field term only (the manifold is "complete" with all the $l_z\ge 3$ states with respect to the Zeeman term). Hence, the coupling is from D to F states.

Schmidt orthogonalization allows to deduce that there are only three even and two odd perturbed states in each k submanifold which depart from the crossed-field hydrogenic behavior. The $(n-\,|\,k\,|\,-5)$ remaining states are still quantized according to the hydrogenic law in agreement with Refs. 18 and 20. The approach is also perfectly suitable for the evaluation of the anticrossing sizes between the nS and perturbed $\{k^*\omega\}$ states.

APPENDIX C: TRANSITION REGION IN THE CROSSED-FIELD DIAGRAM

The transition region (cf. Fig. 3) in the crossed-field energy diagram can be described simply with semiclassical arguments. For the k submanifold (with $n-\,|\,k\,|$ degeneracy) to be insensitive to the incomplete character of the manifold it should be orthogonal to the low-l (S, P, and D) states. This implies that the two following conditions cannot be realized together:

$$j_{1_{\omega_1}}+j_{2_{\omega_2}}=k\ , \tag{C1}$$

$$\|\mathbf{l}\|=\|\mathbf{j}_1+\mathbf{j}_2\|\le 1^*=3\ . \tag{C2}$$

Elementary arguments (see Fig. (2)) allow the evaluation of the minimum value of $\mathbf{l}=\mathbf{j}_1+\mathbf{j}_2$ when $\mathbf{j}_1$ and $\mathbf{j}_2$ are constrained with Eq. (1) and $j_1{}^2=j_2{}^2\simeq n^2/4$. It is realized for $j_{1_{\omega_1}}=j_{2_{\omega_2}}=k/2$ leading to:

$$l_{\min}=\begin{cases} n\,\sin\,[\sin^{-1}(k/n)-\alpha] & \text{if } k/n>\sin\alpha \\ 0 \quad \text{otherwise}\ . \end{cases}$$

Consequently, the crossed-field behavior is no longer of the exact hydrogenic type when $k/n\le\sin[\alpha+\sin^{-1}(l^*/n)]$ [cf. Fig. 3 and Eq. (11)].

Making the approximation $l^*/n\ll 1$, this reads $\omega_s=\frac{3}{2}nE<\Delta_0/n$. The anticrossing disappears below the critical electric field value $E_{\rm cr}=2\Delta_0/3n^2$, in agreement with experiments.

*Present address: L.P.O.C., Tour 12, E05, 4 place Jussieau, 75252 Paris Cedex 05, France.

[1]Recent progress is reviewed, for example, in *Atomic Excitation and Recombination in External Fields,* edited by M. H. Nayfeh and C. W. Clark (Gordon and Breach, New York, 1985).

[2]For example, J. C. Gay, in *Progress in Atomic Spectroscopy,* edited by Beyer and Kleinpoppen (Plenum, New York, 1984).

[3]L. A. Burkova, I. E. Dzyaloshinskii, G. Drukarev, and B. S. Monozon, Zh. Eksp. Teor. Fiz. **71**, 526 (1976) [Sov. Phys.—JETP **44**, 276 (1976)].

[4]H. Crosswhite, U. Fano, K. T. Lu, and A. R. P. Rau, Phys. Rev. Lett. **42**, 963 (1979).

[5]S. K. Bhattacharya and A. R. P. Rau, Phys. Rev. A **26**, 2315 (1982).

[6]E. Korevaar, M. G. Littman, and C. W. Clark, Phys. Rev. Lett. **54**, 320 (1985).

[7]W. Pauli, Z. Phys. **36**, 339 (1926).

[8]V. Fock, Z. Phys. **98**, 145 (1935).

[9]V. Bargmann, Ann. Math. **48**, 568 (1936).

[10]O. Klein, Z. Phys. **22**, 109 (1924).

[11]W. Lenz, Z. Phys. **24**, 197 (1924).

[12]L. C. Biedenharn, Phys. Rev. **126**, 845 (1962).

[13]J. C. Gay and D. Delande, Ref. 1.

[14]D. Herrick, Phys. Rev. A **26**, 323 (1982).

[15]J. J. Labarthe, J. Phys. B **14**, L467 (1981).

[16]J. C. Gay, in *Atoms in Unusual Situation,* edited by J. P. Briand (Plenum, New York, 1986).

[17]C. Chardonnet, D. Delande, and J. C. Gay, Opt. Commun. **51**, 249 (1984).

[18]F. Penent, thèse troisième cycle, Université de Paris, 1984.

[19]F. Penent, D. Delande, F. Biraben, and J. C. Gay, Opt. Commun. **49**, 184 (1984).

[20]P. A. Braun, J. Phys. B **18**, 4187 (1985). Actually, both the method and results are similar to the ones independently established in Ref. 18.

[21]C. Cohen-Tannoudji and P. Avan, Centre National de la Recherche Scientifique International Colloque No. 273 (CNRS, Paris, 1977).

[22]C. Fabre, Y. Kaluzny, R. Calabrese, Liang Jun, P. Goy, and S. Haroche, J. Phys. B **17**, 3217 (1984).

[23]F. Biraben and P. Labastie, Opt. Commun. **41**, 49 (1982).

[24]K. C. Harvey and B. P. Stoicheff, Phys. Rev. Lett. **38**, 537 (1977).

[25]C. J. Lorenzen and K. Niemax, J. Quant. Spectrosc. Radiat. Transfer **22**, 247 (1979).

[26]For example, T. W. Hansen, K. Harvey, G. Meisel, and A. L.

Schawlow, Opt. Commun. **11**, 50 (1974); G. Grynberg and B. Cagnac, Rep. Prog. Phys. **40**, 791 (1977).

[27]B. P. Stoicheff and E. Weinberger, Can. J. Phys. **57**, 2143 (1979).

[28]C. E. Moore, *Atomic Energy Levels,* Natl. Bur. Stand (U.S.) Circ. No. 467 (U.S. GPO, Washington, D.C., 1971), Vol. II.

[29]M. S. O'Sullivan and B. P. Stoicheff, Phys. Rev. A **31**, 2718 (1985).

[30]P. Jacquinot, S. Liberman, and J. Pinard, in Centre National de la Recherche Scientifique International Colloque No. 273 (CNRS, Paris, 1977).

[31]D. Delande, Thèse d'Etat, Université de Paris, 1988.

[32]P. A. Braun and E. A. Solovev, J. Phys. B **17**, L211 (1984).

[33]Y. Demkov, B. S. Monozon and V. N. Ostrovskii, Zh. Eksp. Teor. Fiz. **57**, 1431 (1969) [Sov. Phys.—JETP **30**, 775 (1970)].

[34]A. A. Belov, A. P. Kazantzev, D. V. Khveshchenko, and V. L. Pokrovky, J. Phys. B **18**, 4683 (1985).

[35]E. Korevaar and M. G. Littman, J. Phys. B **16**, L437 (1983).